The Astronomical Journal, 166:64 (14pp), 2023 August https://doi.org/10.3847/1538-3881/ace16b

X-Ray Emission of Ultraviolet Variable Active Galactic Nucleus Candidates

Erik J. Wasleske and Vivienne F. Baldassare
Department of Physics and Astronomy, Washington State University, Pullman, WA 99163, USA; erik.wasleske@wsu.edu
Received 2023 March 10; revised 2023 June 5; accepted 2023 June 22; published 2023 July 17

Abstract

We analyze the X-ray properties of a sample of 23 high-probability active galactic nucleus (AGN) candidates with ultraviolet variability identified in Wasleske et al. Using data from the Chandra X-ray Observatory and XMM-Newton Observatory, we that find 11/23 nuclei are X-ray detected. We use spectral energy distribution modeling to compute star formation rates and show that the X-ray luminosities are typically in excess of the X-ray emission expected from star formation by at least an order of magnitude. Interestingly, this sample shows a diversity of optical spectroscopic properties. We explore possible reasons for why some objects lack optical spectroscopic signatures of black hole activity while still being UV-variable and X-ray bright. We find that host galaxy stellar emission and obscuration from gas and dust are potential factors. We study where this sample falls on relationships such as $\alpha_{OX} - L_{2500}$ and $L_X - L_{IR}$ and find that some of the sample falls outside the typical scatter for these relations, indicating that they differ from the standard quasar population. With the diversity of optical spectroscopic signatures and varying impacts of dust and stellar emissions on our sample, these results emphasize the strength of variability in selecting the most complete set of AGN, regardless of other host galaxy properties.

Unified Astronomy Thesaurus concepts: Active galactic nuclei (16); Active galaxies (17); X-ray photometry (1820); Supermassive black holes (1663); Astrophysical black holes (98)

1. Introduction

It has been well established that black holes (BHs) are ubiquitous in the centers of massive galaxies (Magorrian et al. 1998). Studies of the growth and evolution of supermassive BHs have led to open questions about the occupation and active fractions of BHs. A complete census of active galactic nuclei (AGN) is important for constraining the occupation fraction and studying BH growth throughout time. However, this is difficult to obtain due to selection biases in each wavelength regime across the electromagnetic spectrum, as well as observational limitations. Gas, dust, star formation, and host galaxy dilution each have varying effects on masking the activity of the central BH. This paper is focused on the power of variability selection of AGN for taking a complete AGN census.

The effects of obscuration can be seen across the spectrum of AGN radiation. Absorbing dust emits in the infrared and can mask ultraviolet to infrared emission while, alongside gas, attenuating X-rays (Hickox & Alexander 2018). The lack of luminous X-ray emission in active galaxies that were bright at other wavelengths, such as the infrared, has been shown to be an indicator of heavy obscuration (Donley et al. 2012; Stern 2015; Lambrides et al. 2020; Carroll et al. 2021).

The infrared regime has been explored using photometry in bands spanning 1–1000 μm. Galaxy dust, star formation, and AGN can all dominate the infrared regime. This dust can be heated by either AGN radiation or star formation, making it difficult to differentiate between the two mechanisms by the galaxies' infrared colors (Landt et al. 2008; Kirkpatrick et al. 2015; Hainline et al. 2016). Pfeifle et al. (2022) derived expressions to relate column density to infrared line ratios. They found that obscured AGN have redder mid-infrared (MIR) colors than unobscured systems. Additionally, they found a deficiency of X-ray emission and redder colors for those objects whose host galaxies dominate the 12 μm emission.

Optical spectroscopic studies have been done to collect a large population of active galaxies within the local universe (Ho et al. 1997; Reines et al. 2013). These selection techniques use line ratios and broad emission thresholds. The broad line emission can be obscured by a torus. Studies have shown that the majority of AGN lack broad line emission, i.e., are type II AGN (Villarroel & Korn 2014). The narrow line emission can be affected by dilution from star formation within the host galaxy.

These issues are very prominent in identifying active dwarf galaxies ($M_* < 1 \times 10^{10}\ M_\odot$), whose broad emission lines are fainter and less broad and can often be confused with the signatures of supernovae (Filippenko 1997; Pritchard et al. 2012; Baldassare et al. 2016). Active low-mass galaxies serve as observation tools to constrain the seeding mechanisms of these BHs in the early universe (Volonteri et al. 2008; Volonteri 2010; Natarajan 2014). Populations of active dwarf galaxies have been established using spectroscopic broad and narrow lines (Greene & Ho 2004; Dong et al. 2012; Reines et al. 2013; Moran et al. 2014; Molina et al. 2021), variability (Baldassare et al. 2018, 2020), and X-ray (Greene & Ho 2007; Desroches et al. 2009; Lemons et al. 2015; Plotkin et al. 2016) and radio emission (Reines et al. 2020). These multiwavelength views of active galaxies enable the study of different components of the AGN, but each wavelength regime comes with its own issues and biases. Between decoupling other astrophysical processes from BH activity (i.e., star formation, illuminated gas and dust) and other technical limitations, there is a significant barrier to collecting a complete and accurate sample of AGN. Volume limits create a specific redshift range we can search for active galaxies, with more luminous, less elusive quasars being the only type we are able to systematically search for at the deepest redshifts.

Though X-rays are not immune from obscuration effects, X-ray observations have been well utilized to identify and study the properties of active galaxies (i.e., see Brandt & Hasinger 2005 and references therein). Sufficiently bright X-ray emission is often used to confirm the presence of AGN in systems lacking other AGN indicators (e.g., Birchall et al. 2020; Agostino et al. 2023; Messick et al. 2023, submitted).

Agostino et al. (2023) studied local type 2 AGN selected by X-ray emission that lacked apparent optical emission lines. Even when 25% of their sample spectra was absorption line–dominated, they found measurable [O III] emission in their total sample. The [O III] emits far from the torus of the AGN and can serve as an indicator of AGN power. They found a correlation with the specific star formation rate (SFR) and the [O III] luminosity of these X-ray AGN. Agostino et al. (2023) claimed that less-luminous [O III] galaxies contribute to the scatter of their [O III]–to–X-ray luminosity relation. This scatter is proposed to be from gas content differences of the narrow-line region. They are distinguished only by existing at the low-luminosity ($\log L_X < 42$) end of the broad X-ray–to–[O III] unimodal relation. This separation of less luminous and luminous [O III] emitters is due to the specific SFR. The amount of available molecular gas within the host galaxies drives certain processes, as star formation is dependent on gas, with the photoionization of this gas from the AGN creating its spectroscopic signatures.

Lambrides et al. (2020) also investigated this broad X-ray–to–[O III] relationship for a population of obscured AGN, finding that the type 2 AGN are below the relation of Yan et al. (2011) set for unambiguous AGN. These objects have low observed X-ray emission per their amount of [O III] emission, not from any intrinsic factors but rather from heavy obscuration. Comparison of AGN candidates with varying spectroscopic classes can make indications of the molecular gas contained in the host galaxy.

Correlations of the X-ray to the MIR show a near-linear relation for nearby AGN with low luminosities whose dispersions are attributed to the geometry of the dust, star formation, and variability of the AGN (Lutz et al. 2004; Gandhi et al. 2009). This relationship has been used to convert between X-ray and MIR luminosities regardless of the nature of the AGN, as both uncontaminated MIR and X-ray emission are a proxy for the AGN's intrinsic power (Asmus et al. 2015).

Wasleske et al. (2022) identified 48 AGN candidates by their high variability in the near-ultraviolet (NUV) band. They selected these candidates from 2000 galaxies from the NASA Sloan Atlas (NSA) that lay within the sky covered by the Galaxy Evolution Explorer (GALEX) Time-Domain Survey (TDS; Gezari et al. 2013). The 48 AGN candidates had a variety of optical spectroscopic properties, with some lacking optical spectroscopic AGN signatures entirely. In this paper, we search for nuclear X-ray emission from these UV-variable sources to search for additional evidence of the presence of AGN. Furthermore, we compare their X-ray luminosities to various empirical relations to search for differences between spectral classes. This analysis is compared to the analysis work of Wasleske et al. (2022), who used optical spectroscopy, MIR colors, and low-resolution spectral energy distributions (SEDs). In the analysis of the optical spectra of these variable galaxies, Wasleske et al. (2022) found examples of their variable population having signatures of AGN, star formation, composites, and even absorption line–dominated systems.

This study compares the variable AGN population to known X-ray relations of AGN emission to investigate the underlying physics of their emission signatures. Our goal is to measure X-ray emission from variable AGN candidates and use the multiwavelength galaxy properties to determine whether dust, obscuration, and star formation impact the optical spectral signatures.

This work is structured as follows. In Section 2, we discuss our sample and the data available in the Chandra X-ray Observatory (CXO) and XMM-Newton (XMM) archives. In Section 3, we discuss the data reduction and the construction of SED models. In Section 4, we report our results from the X-ray emission and SED modeling. In Section 5, we discuss the implications of these results in relation to literary observational relations, associating the optical, IR, and X-ray.

2. Data

2.1. Sample Selection

Our sample is comprised of all objects from Wasleske et al. (2022) that had available X-ray data within the CXO or XMM archives. Wasleske et al. (2022) identified 48 high-probability AGN candidates from their NUV variability in the GALEX TDS (Gezari et al. 2013). The parent population for this variability study was taken from the NSA, which combines imaging products from the Sloan Digital Sky Survey (SDSS) and GALEX to construct a catalog of roughly 641,500 galaxies with redshifts and other derived quantities (Blanton & Moustakas 2009; Maller et al. 2009; Zhu et al. 2010). There were ∼2000 galaxies in the region covered by GALEX TDS that were analyzed for their NUV variability. The 48 high-probability candidates were selected for significant variability in their light curves over the 3 yr baseline of the TDS. The pointing of the TDS covered six of the Pan-STARRS1 Medium Deep Survey fields, four of which are in the northern sky. The NUV filter covers a range from 1750 to 2800 Å.

Of the 48 AGN candidates, 23 unique objects had coverage with either the CXO or XMM archive. The description of these data products is given below.

2.2. Chandra X-ray Observatory

We searched for 48 AGN candidates from Wasleske et al. (2022) in the CXO archive. To establish whether the objects were observed with Chandra, we searched for each object in the Chandra archive with a default search radius of 10′. We then examined each observation to determine whether the object was contained within the field. We found a total of 13 objects covered by Chandra ACIS observations, with some objects having repeat observations. The reduction of these observation products is described in Section 3.1. Galaxy NSA 64129 is the only one that was not analyzed. It is 9.′07 from the nearest observation's center, and inspection of that observation's image shows that the galaxy straddles the edge of the CCD; thus, we removed it from the CXO sample. However, NSA 64129 lies within the XMM Source Catalog, as discussed in Section 2.3. A cross-check of the Chandra Source Catalog, CSC 2.0 (Evans et al. 2020), was done to ensure that the appropriate data products were collected from the archive for the remaining 12 objects.

Our sample of 12 objects having CXO observations has an array of optical spectroscopic signatures that were analyzed in Wasleske et al. (2022). From the BPT diagram (Baldwin et al. 1981), two objects are classified as AGN, one as a starburst and

Table 1
Our Sample from Wasleske et al. (2022) of UV-variable AGN Candidates Found in X-Ray Surveys

X-Ray Sample				CXO			XMM	
NSA ID	z	$\log(M_*/M_\odot)$	BPT Class	Counts	n_H (10^{22} cm^{-2})	$L_{0.5-7.0\ keV}$ [erg s^{-1}]	n_H (10^{22} cm^{-2})	$L_{0.5-7.0\ keV}$ (erg s^{-1})
28616	0.0991	10.89	AGN	⋯	⋯	⋯	0.106	$2.8^{+0.1}_{-0.09} \times 10^{43}$
28810	0.1394	11.24	None	$\leqslant 15 \pm 4$	⋯	$<8.6 \times 10^{41}$	⋯	$<7.7 \times 10^{41}$
64129	0.0783	10.53	AGN	⋯	⋯	⋯	0.096	$5.0^{+0.5}_{-0.5} \times 10^{41}$
64145	0.1030	10.59	Absorption	1397 ± 37	2.230	$(3.6 \pm 0.7) \times 10^{42}$	0.045	$(1.2 \pm 0.3) \times 10^{42}$
64258	0.1084	10.74	Starburst	$\leqslant 8 \pm 2$	⋯	$<7.3 \times 10^{39}$	⋯	$<2.1 \times 10^{41}$
64266	0.0805	10.68	None	$\leqslant 12 \pm 4$	⋯	$<6.5 \times 10^{39}$	⋯	$<1.5 \times 10^{41}$
64272	0.1329	10.89	AGN	554 ± 24	⋯	$(4.6 \pm 0.3) \times 10^{42}$	0.107	$(9.7 \pm 0.2) \times 10^{42}$
64286	0.0234	10.67	AGN	97 ± 10	1.667	$2.7^{+3.4}_{-0.7} \times 10^{41}$	0.036	$(5.3 \pm 0.2) \times 10^{41}$
205160	0.1396	10.52	None	⋯	⋯	⋯	⋯	$<1.3 \times 10^{42}$
208465	0.0765	11.61	Absorption	⋯	⋯	⋯	0.055	$(2.4 \pm 0.03) \times 10^{43}$
208625	0.0732	10.85	Absorption	503 ± 22	⋯	$1.4^{+0.6}_{-0.7} \times 10^{42}$	⋯	$<1.4 \times 10^{41}$
208662	0.1122	10.98	Composite	455 ± 21	2.49	$8.4^{+10.1}_{-7.0} \times 10^{40}$	⋯	$<1.2 \times 10^{42}$
208702	0.0448	9.61	Composite	⋯	⋯	⋯	⋯	$<9.9 \times 10^{40}$
259478	0.0784	10.84	Composite	⋯	⋯	⋯	⋯	$<1.7 \times 10^{41}$
259789	0.1063	10.76	None	10038 ± 100	0.292	$4.9^{+3.1}_{-2.5} \times 10^{40}$	⋯	⋯
259880	0.0762	10.65	Absorption	⋯	⋯	⋯	⋯	$<1.3 \times 10^{41}$
259895	0.0834	10.11	AGN	⋯	⋯	⋯	0.226	$(2.4 \pm 0.2) \times 10^{42}$
259919	0.0781	10.52	Absorption	⋯	⋯	⋯	⋯	$<1.2 \times 10^{41}$
260221	0.0742	10.73	Absorption	⋯	⋯	⋯	⋯	$<2.1 \times 10^{41}$
260241	0.0743	10.51	None	⋯	⋯	⋯	⋯	$<1.5 \times 10^{41}$
613397	0.1274	11.54	Absorption	$\leqslant 9 \pm 3$	⋯	$<3.3 \times 10^{41}$	⋯	⋯
631480	0.0442	7.74	None	$\leqslant 5 \pm 3$	⋯	$<9.8 \times 10^{38}$	⋯	$<3.6 \times 10^{40}$
631492	0.0119	6.89	None	25 ± 5	⋯	$7.8^{+10.8}_{-6.7} \times 10^{37}$	⋯	$<8.0 \times 10^{39}$

Note. Counts for CXO detections are calculated by their 0.5–7.0 keV count rate multiplied by the exposure time, with Poissonian errors given. Their BPT classifications are given as "BPT Class," with some spectra dominated by absorption lines. Those galaxies with a BPT Class of "none" do not have available spectra that can be properly fitted and analyzed. Intrinsic absorption n_H values are given for detections in CXO and XMM based on the methods described in Sections 3.1 and 3.2.

one as a composite galaxy. Three of the objects are dominated by absorption features, while the rest either have no available SDSS spectrum or the spectrum is too noisy to perform the fitting routine.

2.3. XMM-Newton Observatory

We searched the XMM Serendipitous Source Catalog (Webb et al. 2020) for matches to our 48 AGN candidates from Wasleske et al. (2022). Beyond collected detections, we searched for upper limits of the remaining galaxies within XMM's coverage.

The 4XMM-DR9 catalog is based on a set of 11,204 EPIC observations spanning 19 yr that contain a detection. Data processing for this catalog was based on Science Analysis Software (SAS) version 18 to produce calibrated event lists for each observation. The process of converting the raw observation data event files from the EPIC instruments into event lists by the pipeline is the same as described in Watson et al. (2009). The 4XMM-DR9 updates to the 2XMM (Watson et al. 2009) and 3XMM (Rosen et al. 2016) catalogs are the inclusion of source spectra, light curves, source detection, and event corrections using timing mode and pn small-window data. This catalog contains 550,000 unique sources, building upon earlier iterations with improved source detection, and provides ideal easy access to data products from the XMM archive. Webb et al. (2020) discussed the properties of the catalog, finding a Gaussian distribution of fluxes for all sources detected. The minimum flux value for the 0.2–12 keV broadband is 1.44×10^{-19} erg cm^{-2} s^{-1} for source 4XMM J174538.0–285950.

This catalog contains fluxes in nine X-ray bands for each object that span different pieces of the 0.2–12keV energy range. Analysis of the selected sources is described in Section 3.2. Of the 48 variable AGN candidates, seven were found in the source catalog. Selection and analysis of these sources is discussed in Section 3.2.

Using the FLIX server,[1] we compute X-ray upper limits for an additional 14 of the AGN candidates from Wasleske et al. (2022), given in Table 1. These 14 objects were within fields observed by XMM, but the separation between the nearest detected source within the catalog and each of these candidates was within the range of 50″–207″. Seven of these objects were also found in the CXO archive. We compute upper limits using the pn band 8 (0.2–12.0 keV) flux from the observation with the minimum axis offset value for each of these 14 candidates.

2.4. Ancillary Data

Photometry was collected from surveys across the electromagnetic spectrum to be used for input values of the SED models. Along with the photometric X-ray values pulled from our analysis, we use the median GALEX photometric values from Wasleske et al. (2022) for each variable galaxy, data from

[1] http://flix.irap.omp.eu/

SDSS DR16 (Ahumada et al. 2020), the United Kingdom Infrared Telescope (Lawrence et al. 2007), the Wide-field Infrared Survey Explorer (WISE; Wright et al. 2010), unblurred and unofficial coadds of the WISE imaging (Lang 2014), and the Two Micron All-Sky Survey (Skrutskie et al. 2006).

The compilation of these values serves as the input of the SED analysis using X-CIGALE V2022.0 (Yang et al. 2022), discussed in Section 3.3.

3. Analysis

We present an examination of the reduction and compilation of X-ray data to measure broadband photometric luminosities. We also discuss the process and the choices made for the SED modeling.

3.1. CIAO Reduction

The Chandra Interactive Analysis of Observations (CIAO; version 4.14[2]) data reduction software was used to reduce and analyze the observations. For each observation file, we first reprocessed the observation files using the chandra_repro script to apply the latest calibrations, which creates a new level 2 event file and a bad-pixel file from the background cleaning of the original event file. Preliminary sources within the level 2 event file are then identified using the CIAO WAVDETECT function. WAVDETECT does this through correlating potential pixel sources to Ricker wavelet functions, removing highly correlated values as assumed sources. After this is completed, we filter the event file to the 0.5–10.0 keV range.

We used CIAO's SRCFLUX software to carry out the aperture photometry. The SRCFLUX software calculates net count rates and fluxes with uncertainties while accounting for contributions of the point-spread function to both source and background apertures. We use a $2\farcs0$ source aperture in unison with a sourceless background annulus of size $20\farcs00$ for its inner and $30\farcs00$ for its outer radius. Our source aperture is set by the spatial resolution of the CXO.

The spectral model we used within the SRCFLUX[3] function for all CXO objects is xsphabs.abs1 *xspowerlaw.pow1, where xspowerlaw is a simple photon power law where we defined its index as $\Gamma = 1.8$. This model only accounts for galactic absorption, not the host galaxy of each for these sources. We set the absorption parameter to abs1.nH=%GAL% so that National Radio Astronomy Observatory values for the galactic column density $n_{\rm H}$ are collected.

Assuming this absorbed power-law spectrum, we then collect count and flux estimates for broad (0.5–7.0 keV), soft (0.5–1.2), medium (1.2–2.0 keV), and custom (2.0–10.0 keV) bands. Once these estimated values are collected, we follow the method of Baldassare et al. (2017) to measure the intrinsic absorption. Using the Portable Interactive Multi-Mission Simulator (PIMMS) toolkit,[4] we started with our custom 2.0–10.0 keV band's count rate to calculate the expected count rate for the 0.5–2.0 keV band, assuming a photon index of $\Gamma = 1.8$. If this expected value was higher than the observed rate from the CIAO reduction, an intrinsic $n_{\rm H}$ was calculated. This was the case for four of the objects detected in CXO, with the intrinsic $n_{\rm H}$ value given in Table 1.

From these fluxes, we calculate the luminosities using the distances given in the NSA.

The bottom panels of Figure 1 show the source and background apertures over each event file used in the data reduction. For NSA 64286, as the object was collected near the edge of the ACIS chip, the background annulus aperture was centered at R.A. $= 150\fdg500$, decl. $= 3\fdg077$, $2\farcm1$ away from the object's position and the source aperture. Analogous optical legacy imaging cutouts are given in the top panels of Figure 1.

3.2. XMM Source Catalog Objects

Sources from the XMM Serendipitous Source Catalog were cross-matched to the AGN candidates via closest 2D sky separation. This list was then filtered down to a more probable comparison if the sources were within a $10''$ radius of the object's position. This separation threshold filtered the list down to seven probable sources, three of which overlap with our CXO sample. Figure 2 shows the positions of the sources compared to the position given in the NSA catalog. The $6''$ resolution of the XMM instrument is given by the black circles in each panel of Figure 2. This demonstrates the accuracy of the 2D position cross-matching used to select these sources. We collect the 0.2–12 keV fluxes for these seven sources.

Once these sources were identified, we used the spectrum fitting tool[5] for source and respective detection IDs for these source to fit the broadband 0.2–12.0 keV spectrum. This fitting gave a total absorption estimate for the spectrum. Since we know the Galactic absorption for each position, we can then compute the intrinsic absorption of each object. These values are given for the XMM source detections in Table 1.

The 0.5–7.0 keV broadband luminosity for these X-ray analogous sources and the FLIX upper limits are given in Table 1. The PIMMS toolkit was used to convert the broadband luminosity of 0.2–12 keV to the broad 0.5–7.0 keV CXO band for ease of comparison.

3.3. SED Modeling

Using X-CIGALE V2022.0 (Yang et al. 2022), we fit SED models to estimate the emission mechanisms for all 23 objects. The photometric values, including those for the GALEX NUV band, are equivalent to those used in the Wasleske et al. (2022) SED decomposition, with the addition of the X-ray values collected above. The X-ray boxcars for the ranges of 0.5–7.0 and 0.2–12.0 keV were used for the CXO and XMM sources, respectively. We followed the SED-fitting methodology of Burke et al. (2021) to set the specific models and parameter ranges for our SED models. The Burke et al. (2021) SED analysis focused on modeling galaxies whose SEDs were not dominated by the central AGN, which is well aligned with the sample and science goals presented here. We detail this work below.

To model the AGN emission, we use the SKIRTOR (Stalevski et al. 2012, 2016) model for its two-phase clumpy model of the radiative transfer of the AGN's dusty torus. We let the AGN fraction vary from 0.0 to 0.9 and the polar extinction $E(B-V)$ maximum value be 0.175. The viewing angle was allowed to vary between 10° and 60°.

[2] See https://cxc.cfa.harvard.edu/ciao/ for user guides for this software package.

[3] SRCFLUX references its models from Xspec; see https://heasarc.gsfc.nasa.gov/xanadu/xspec/manual for user manual.

[4] https://heasarc.gsfc.nasa.gov/docs/software/tools/pimms.html

[5] See "Fit Spectrum" option of http://xmm-catalog.irap.omp.eu/.

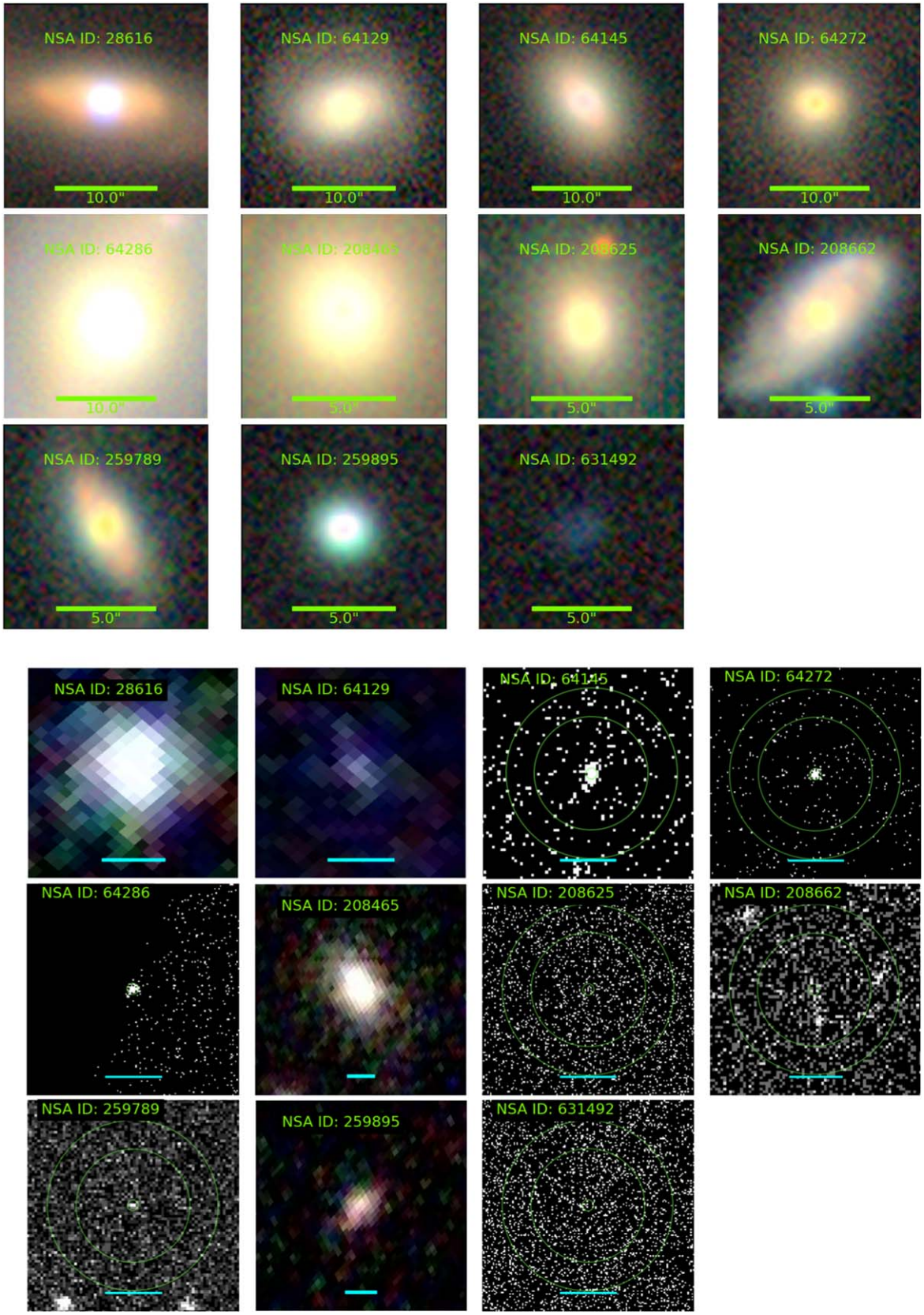

Figure 1. Top: Legacy Survey images of the galaxies from our sample with X-ray detections in either CXO and XMM. Bottom: X-ray images for each galaxy with an X-ray detection. The teal scale bar is 20″ on each panel. For objects detected with XMM (i.e., NSA 28616, 64129, 208465, and 259895), the XMM EPIC-RGB cutout is shown. Collected from http://xmm-catalog.irap.omp.eu/. For objects detected in CXO, the circular source aperture and annulus background aperture from the CIAO data reduction are given in green. For those detected in both CXO and XMM, the CXO image is displayed.

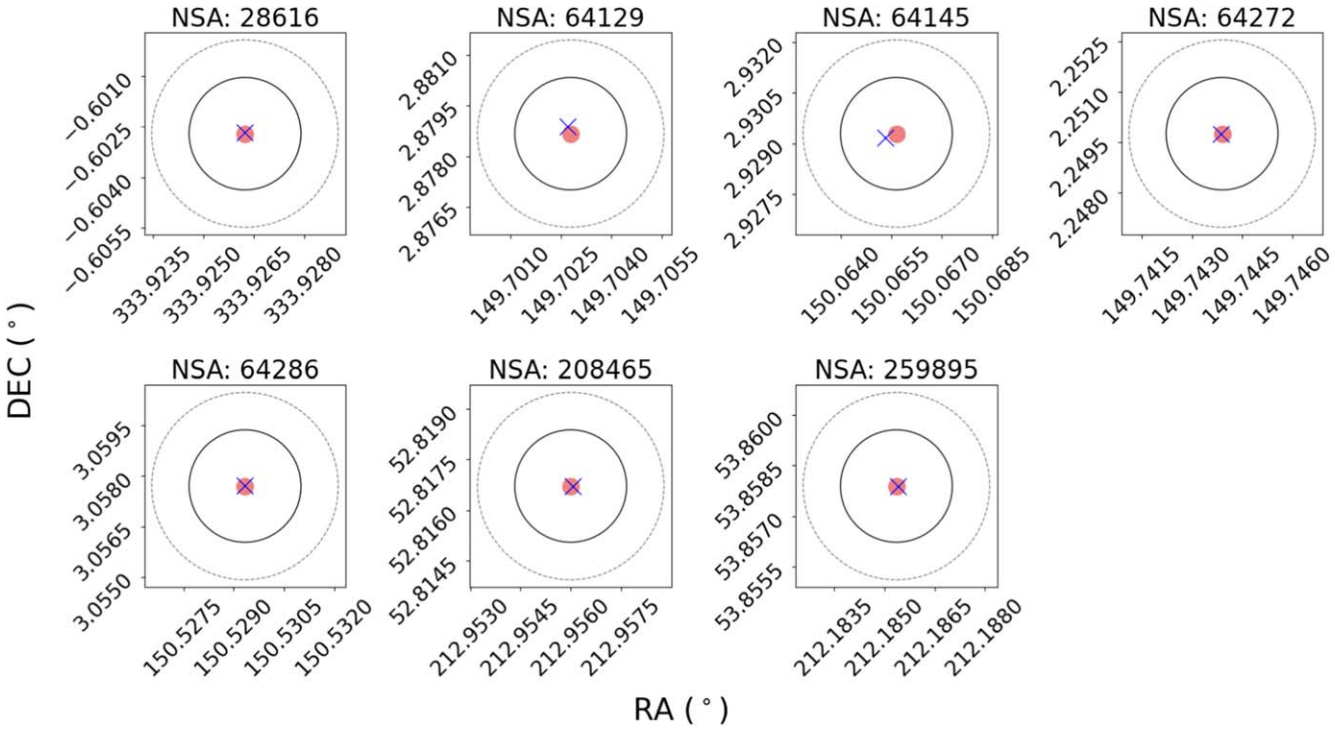

Figure 2. The X-ray source and object positions for sources found in the XMM catalog. Faint red circles show the object position, while the blue cross represents the X-ray source position. The solid black circle represents the 6″ FWHM point-spread function of XMM. The 10″ threshold circle is given in dashed gray.

The star formation history was done using a delayed exponential model. This model used the parameters of e-folding times ranging from 100 to 5000 Myr and an age of the main stellar population of 1000, 2000, or 5000 Myr. We used the initial stellar mass function from Chabrier (2003), the stellar population models of Bruzual & Charlot (2003), and the nebular emission model of Inoue (2011). Dust emission was modeled by Draine et al. (2013), with extinction reddening from the Calzetti et al. (2000) template. Example SED models are given in Figure 10 in the Appendix.

4. Results

We present the results of the data reduction processes stated above.

4.1. X-Ray Properties

Broadband 0.5–7.0 keV X-ray luminosities are given in Table 1 for the 23 objects covered by CXO and/or XMM. The X-ray luminosities range from $L_{0.5\text{–}7.0\ \mathrm{keV}} = 7.8 \times 10^{37}$ to 2.8×10^{43} erg s^{-1}. Of the 23 galaxies with X-ray coverage in either CXO or XMM, 11 are detected in the X-ray. Figure 3 plots the relationship of stellar mass to 0.5–7.0 keV luminosity for both XMM and CXO sources.

Through the CXO data reduction for 12 objects, we found X-ray luminosities ranging from $L_{0.5\text{–}7.0\ \mathrm{keV}} = 7.8 \times 10^{37}$ to 4.6×10^{42} erg s^{-1}. There were two dwarf galaxies with CXO coverage: NSA 631492 and 631480. The stellar mass range of objects from the CXO archive is $\log(M_*/M_\odot) = 6.89$–11.54.

Upper limits were found for NSA 28810, 64258, 64266, 613397, and 631480 within the CXO observations. Their values range from 9.8×10^{38} erg s^{-1} for NSA 631480 to 8.6×10^{41} erg s^{-1} for NSA 28810.

The X-ray luminosities for the XMM Source Catalog objects are generally higher than for those observed with CXO. The X-ray luminosity range is $L_{0.5\text{–}7.0\ \mathrm{keV}} = 5.3 \times 10^{41}$ to 2.8×10^{43} erg s^{-1}. The catalog sources are all massive galaxies with a stellar mass range of $\log(M_*/M_\odot) = 10.53$–$11.61$.

Upper limits from XMM observations were found for NSA 28810, 64258, 64266, 205160, 208625, 208662, 208702, 259478, 259880, 259919, 260221, 260241, 631480, and 631492. Their values range from 8.0×10^{39} to 1.3×10^{42} erg s^{-1}. We note that these provide loose constraints on the luminosity of the objects, as these limits are derived from flux upper limits of the observations themselves.

At $L_{0.5\text{–}7.0\ \mathrm{keV}} = 7.8 \times 10^{37}$ erg s^{-1}, NSA 631492 has the lowest luminosity of our whole X-ray population. It is also worth noting that NSA 631492 is the least massive object in this study at $\log(M_*/M_\odot) = 6.89$, and it lacks an optical spectrum from SDSS. In contrast, the most massive galaxy, NSA 208465, with a stellar mass of $\log(M_*/M_\odot) = 11.61$, is the second most luminous within our population. Its optical spectrum is dominated by absorption lines.

We find that three of the seven X-ray sources within CXO are moderately obscured, with intrinsic n_{H} on the order of 10^{22} cm^{-2}. Comparatively, all of the XMM sources are below this threshold of obscuration, pointing to the bias of the XMM Source Catalog toward bright AGN.

Figure 3 shows the stellar masses versus $L_{0.5\text{–}7.0\ \mathrm{keV}}$ for each target. We observe a general trend that an increase in host stellar mass leads to an increase in X-ray luminosity. Objects with both CXO and XMM luminosities are marked in the figure. These cases are discussed further in Section 4.2.

4.2. Objects Detected with CXO and XMM

As seen in Table 1, NSA 64145, 64272, and 64286 have both bright X-ray emission within archival CXO data and an

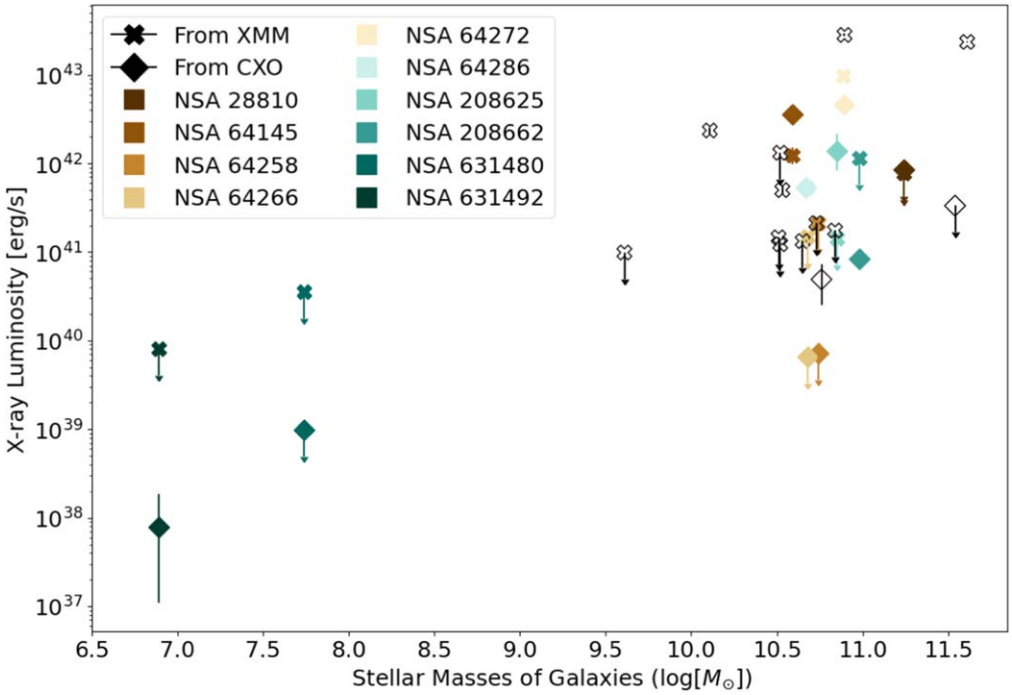

Figure 3. Galaxy mass vs. X-ray luminosity for each source and upper limit. Diamonds represent values collected from CXO, with crosses representing XMM. We color-coordinated points from XMM and CXO to represent a singular object. Open points represent objects with values taken from only one survey.

associated source within the XMM Source Catalog. Thus, we can evaluate whether these sources have persistent or variable/transient X-ray emission. We present the GALEX NUV light curves for these three objects from Wasleske et al. (2022) in Figure 4.

We find consistent and persistent broadband X-ray emission for NSA 64145, 64272, and 64286. For NSA 64145, the CXO observations were taken in 2013 June, and the XMM observations were taken between 2004 December and 2006 May. Thus, NSA 64145 demonstrates persistent X-ray emission over a nearly decade-long timescale. Object NSA 64286 also has consistent X-ray luminosity between its XMM and CXO observations, taken in 2015 May and 2019 March, respectively. For NSA 64272, both its CXO and XMM X-ray luminosities are roughly consistent, within a half dex of each other. The XMM Source Catalog used observations from 2003 December, 2006 May, and 2007 May. The CXO observation for this object was taken in 2007 January.

We consider the X-ray emission from the three sources above to be most likely due to an AGN, as opposed to a variable source such as a tidal disruption event (TDE). The TDEs would not be visible in the optical spectrum beyond a timescale of months to a year. Faint and fast TDEs are seen to peak within a month and decline in a shorter time (Charalampopoulos et al. 2023). Optical and X-ray emission from TDEs is typically seen over a months-long timescale (Rees 1988; Komossa et al. 2008; Strubbe & Quataert 2009; Wang et al. 2012; Cao et al. 2018; see Gezari 2021 for a review and references therein).

Objects NSA 28810, 64258, 64266, 208662, 631480, and 631492 each have analogous XMM upper limits paired with their CXO detection or upper limit. In these cases, if the object is detected by CXO, the CXO X-ray luminosity is less than the XMM upper limit.

Interestingly, NSA 208625 has a CXO detection at a higher value than its XMM upper limit. All archival CXO observations of this object were taken between 2005 August and October. The XMM observed this field on 2015 December 26. The UV light curve, constructed with data collected between 2009 May 4 and 2011 March 14, shows stochastic variability rather than a burst-like light curve. A possible scenario for this object is a TDE that occurred prior to the CXO observations and faded by the time of the XMM observations. The intermediate UV variability could be from residual accretion following the TDE. Alternately, this object could be a changing-state AGN. Further study of this object is needed to confirm either scenario.

5. Discussion

We compare the X-ray luminosities to different host galaxy properties estimated by the SED modeling. We show that the X-ray luminosities are higher than would be expected based on SFRs. We compare these objects against known relationships for luminous quasars and search for reasons why these UV-variable, X-ray-bright AGN candidates can lack optical signatures of BH activity.

5.1. Origin of X-Ray Emission

We can compare the X-ray emission to the SFRs as estimated by the SED models as an additional confirmation of the presence of an AGN. Ranalli et al. (2003) developed a relation between SFR and hard X-ray luminosity for normal (non-AGN) galaxies. This relation reflects the expected X-ray emission from X-ray binaries and supernova remnants. An excess of X-ray emission for a galaxy's SFR can indicate the presence of an AGN in a galaxy. This relationship was used by Agostino et al. (2021) to identify AGN candidates.

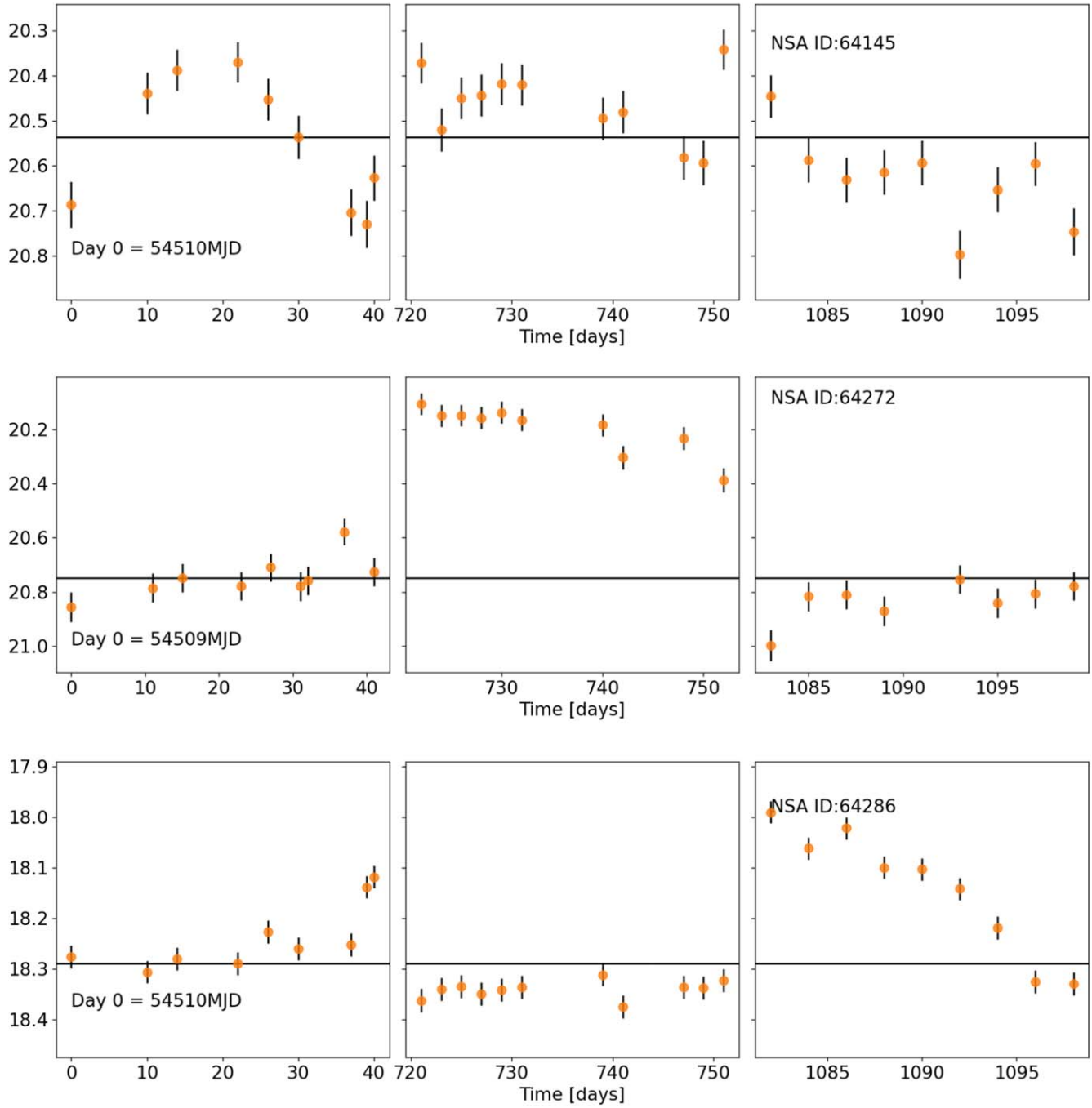

Figure 4. Top: GALEX NUV light curve of NSA 64145 from Wasleske et al. (2022). Middle: GALEX NUV light curve of NSA 64272. Bottom: GALEX NUV light curve of NSA 64286. Each of these light curves show significant (>0.2 mag) variability across roughly 3 yr. Objects NSA 64272 and 64286 show a significant change in mean magnitude in one of their observation windows for a duration of about a month. Thus, we investigate the possibility of a TDE in Section 4.2.

We plot the estimated SFR from SED modeling versus $L_{0.5-10\ \mathrm{keV}}$ for our sample in Figure 5. Almost every galaxy in our sample is shown to have excess X-ray emission compared to the Ranalli et al. (2003) relation for non-AGN objects. The notable exception is NSA 631492, which is the lowest-mass, lowest X-ray luminosity object in the sample.

Agostino et al. (2023) found that LINER-type galaxies have excess X-ray emission across broad 0.5–10 keV for their SFR compared to normal non-AGN galaxies. They separated their X-ray AGN candidates as those having X-ray luminosities more than 0.6 dex above the X-ray luminosity predicted from their SFR. All but NSA 631492 lay within the Agostino et al. (2023) criteria for X-ray AGN.

Even the galaxies with star formation, composite, and absorption line–dominated optical spectra in our sample have X-rays in excess of the SFR predictions. The galaxies with optical spectroscopic AGN signatures have a higher excess of X-ray emission compared to the spectroscopic star-forming and composite galaxies. Our results are similar to those of Agostino & Salim (2019), who found that some of their X-ray AGN candidates did fall within the star-forming region of the BPT diagram. Agostino et al. (2023) also found that one-quarter of their X-ray AGN sample had apparent pure absorption-

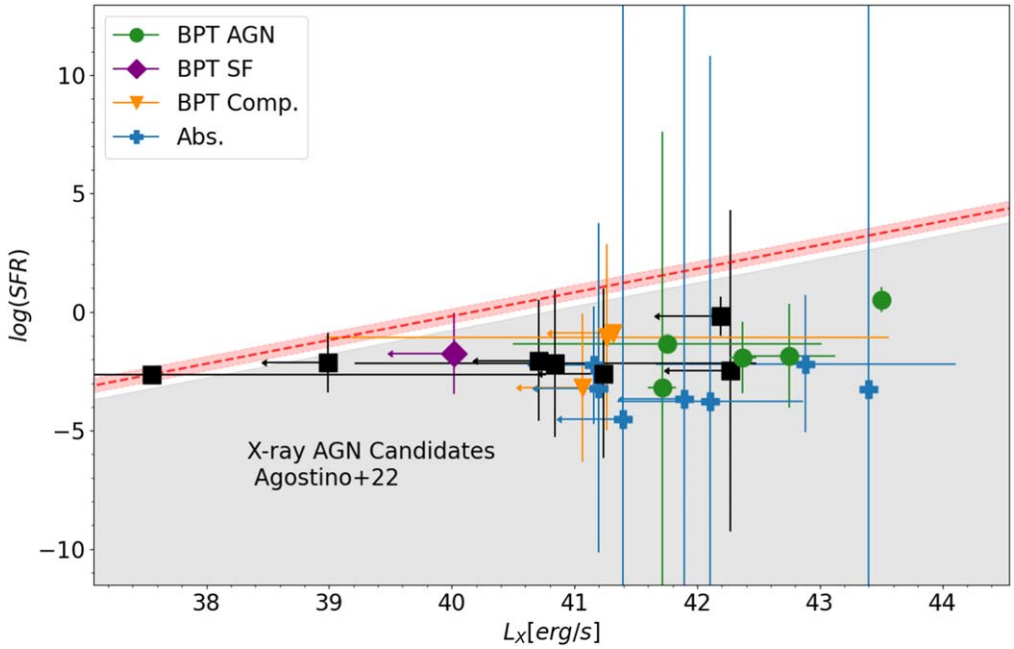

Figure 5. The SFR vs. 0.5–10 keV X-ray luminosity. The SFRs are the Bayesian SFRs estimated from our SED modeling. The relation between SFR and X-ray luminosity for normal galaxies is defined by Ranalli et al. (2003). Agostino & Salim (2019) adapted this relation for 0.5–10 keV X-ray luminosities. The dashed red line shows this adaptation, with the shaded red region quoting the intrinsic scatter of 0.3 dex (1σ) found by Ranalli et al. (2003). The gray shaded region reflects the selection criteria for X-ray AGN from Agostino et al. (2021, 2023), where AGN candidates are chosen to have an X-ray excess of $\geqslant$0.6 dex compared to the Ranalli et al. (2003) relation. Green dots, purple diamonds, and orange triangles represent BPT AGN, star-forming, and composite classifications on the BPT diagram (Baldwin et al. 1981), respectively. These values are taken from Wasleske et al. (2022). Blue plus signs represent absorption line–dominated spectra. Black squares represent galaxies that either did not have optical spectra or had spectra that could not be fit.

dominated spectra. However, it is possible that higher-resolution optical spectra (compared to SDSS spectroscopy) or more robust optical spectroscopic modeling would reveal some AGN signatures.

All of the X-ray-detected objects besides NSA 631492 are likely AGN based on having UV variability and X-ray emission in excess of SFR-based expectations. This includes all five BPT AGN, $1/3$ BPT composites, $3/7$ absorption line systems, and $1/7$ of the galaxies with no optical spectroscopy. For the nondetected objects, the upper limits are generally not constraining enough to rule out the possible presence of an AGN.

These results demonstrate that variability selection is as effective as X-ray selection at identifying AGN in objects lacking optical spectroscopic signatures.

5.2. Diversity of Optical Spectroscopic Properties

Through our X-ray analysis, we establish that almost all of the UV variability–selected, X-ray-detected objects are bona fide AGN. In this section, we discuss possible explanations for the diversity in optical spectroscopic signatures.

5.2.1. Stellar Populations

Here we investigate the AGN power versus the emission from stars as estimated by our SED modeling. We note that all of the objects in our sample preferred an AGN to be included in the best-fit SED. For galaxies without optical spectroscopic AGN signatures, it is possible that host galaxy stellar light is diluting the AGN emission. Stellar and AGN emission can also both heat dust. In Figure 6, we show the best-fit stellar versus AGN luminosity from SED modeling. For the full sample, the stellar population is brighter than the AGN. However, the stellar population is more dominant for the absorption line–dominated systems than for the AGN or composite objects. This is notable, as the X-ray emission from the absorption line systems is comparable to the BPT AGN, suggesting that it is not simply a question of AGN power. This suggests that host galaxy stellar populations or heating of dust by stellar emission could be diluting the AGN signatures for these objects.

5.2.2. Disk–Corona Relation

Just et al. (2007) investigated the correlation of the X-ray–to–optical slope $\alpha_{\rm OX}$ to monochromatic luminosity density $l_{2500\text{Å}}$ for luminous quasars in the SDSS. They found a clear dependence of $\alpha_{\rm OX}$ on this UV luminosity and no significant change in the $\alpha_{\rm OX}$ over the redshift range of $1.5 \leqslant z \leqslant 4.5$. We explore whether our sample also follows the $\alpha_{\rm OX}$ relation in Figure 7. Points are identified by their location on the BPT diagram. Residuals to the Just et al. (2007) relation are given in the bottom panel.

Inspection of Figure 7 shows that the subpopulation with optical spectroscopic AGN signatures best agrees with the Just et al. (2007) relation, whereas the BPT composite and star-forming galaxies, absorption line systems, and those with no optical spectroscopy deviate more significantly from this relation.

As the hard X-rays of AGN come from the innermost region of the accretion disk, deviations below the relationship from Just et al. (2007) suggest the presence of obscuring material. This obscuring material can affect not only these potential type II AGN but also low-luminosity type Is. This obscuring gas could be highly ionized, having no significant dust grains due

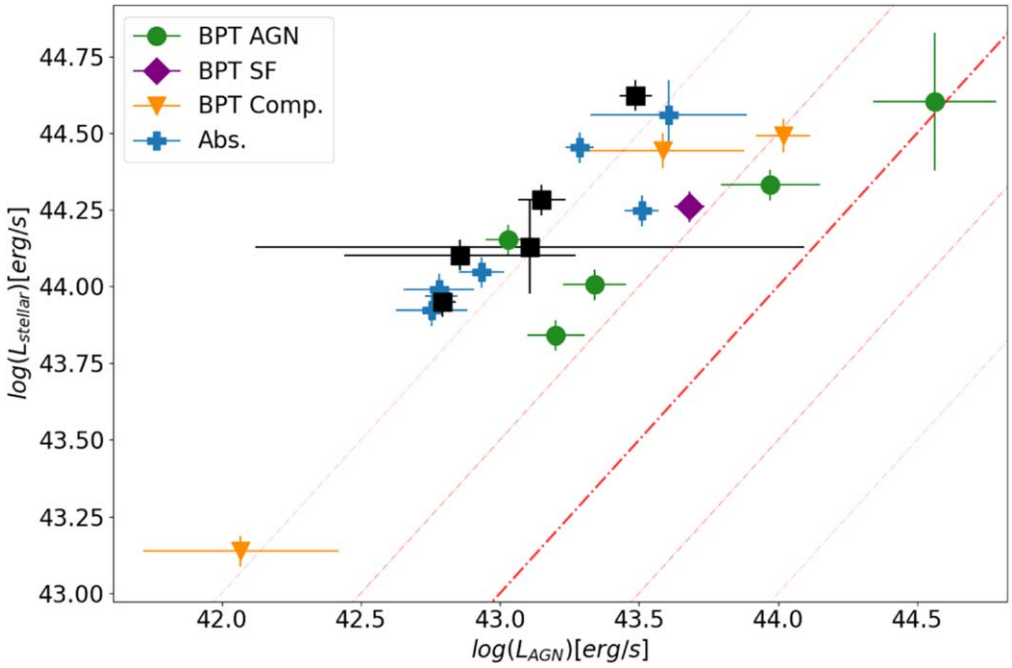

Figure 6. Scatter plot of AGN to stellar luminosity measured from SED modeling. The thick red dashed–dotted line is the unity line. The other faint red curves are 0.5 dex deviations from unity. Points for NSA 631492 and 631480 are left off, as they exist in the far left, less luminous regime, compared to the rest of the sample. Marker shapes and colors are the same as in Figure 5.

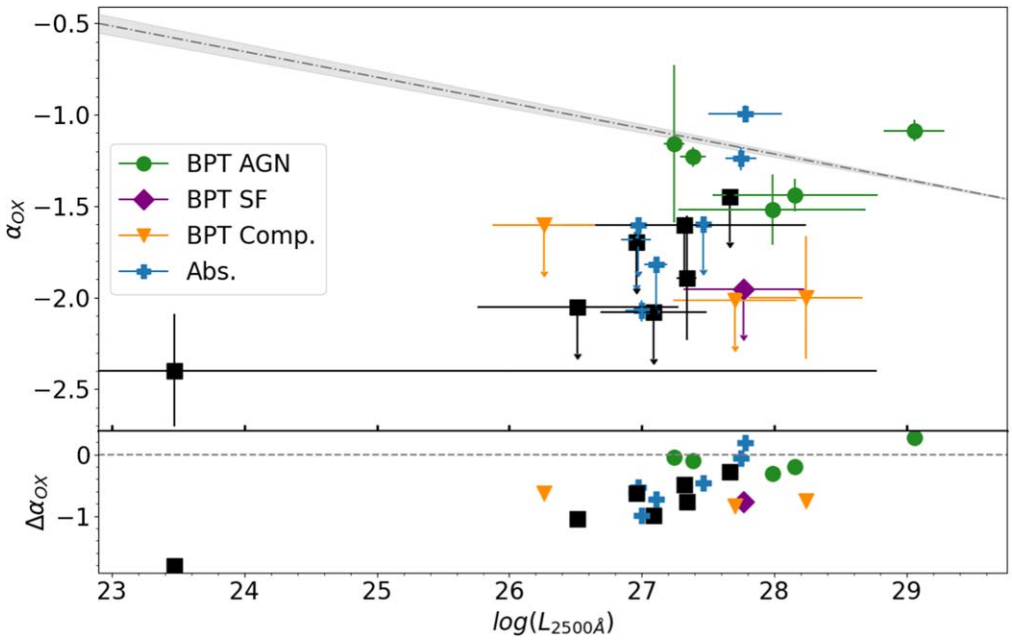

Figure 7. Comparison of α_{OX} to monochromatic luminosity at 2500 Å. The relation derived for quasars from Just et al. (2007) is plotted as the gray line. Residuals from the Just et al. (2007) relation are given in the bottom panel. The BPT AGN have the tightest fit to this relation. Marker shapes and colors are the same as in Figure 5.

to the heating from the accretion outflow. High-resolution spectroscopy of less luminous sources, such as NSA 631492 and 631480, would help decipher whether this object is a type II or low-luminosity type I AGN. We further investigate the effects of dust in Section 5.2.3.

The deviation from α_{OX} for these nonspectroscopic AGN could also suggest a low ionization parameter, ξ, of its accretion disk.

We note that some objects with absorption features in their optical spectra have a closer correspondence than other non-BPT AGN. With optical absorption features suggesting a predominantly older stellar population, the bright X-ray emission of these sources paired with their UV variability supports the need for additional multiwavelength observations for these objects to fully understand the processes at work.

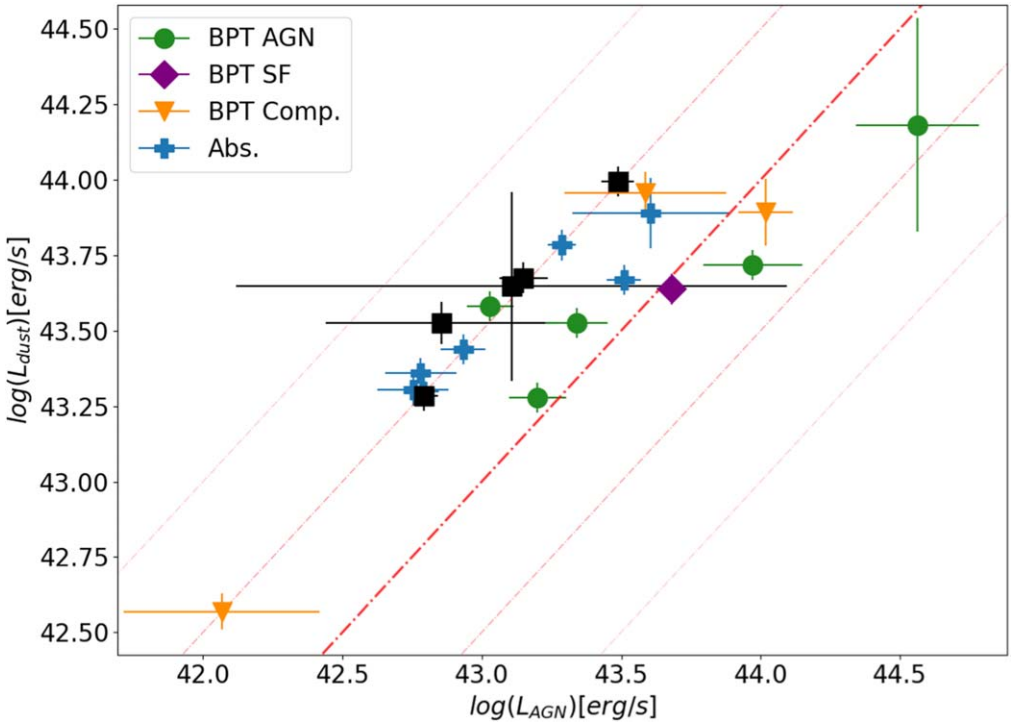

Figure 8. Plot of AGN vs. dust luminosity for our sample. Lines are the same as in Figure 6. Again, the points for NSA 631492 and 631480 are left off, as they exist in the far left, less luminous regime, compared to the rest of the sample. Marker shapes and colors are the same as in Figure 5.

5.2.3. Dust Obscuration

We investigate the potential effect of dust obscuration from the host galaxy on the spectroscopic signatures of our sample. Narrow emission lines are known to to be attenuated by dust (see Hickox & Alexander 2018 and references therein). Rigby et al. (2006) found that dust obscuration from the host galaxy is a likely cause of optically dull emission line ratios.

For our sample, we find that the dust-to-AGN luminosity plot of Figure 8 separates these objects similarly to the distinction of Figure 6, as the absorption line–dominated and non-BPT AGN have higher dust luminosities than the rest of the sample. However, there is less of a spread in dust luminosities than is seen for stellar luminosities.

5.2.4. Excess MIR Luminosity

Previous works have used the relationship between MIR and X-ray luminosity to explore the accretion physics and dust structure of luminous AGN. Gandhi et al. (2009) established a tight linear relation between MIR and X-ray luminosity for local Seyfert galaxies. Rigby et al. (2006) investigated the MIR emission of their sample, finding that their optically dull X-ray AGN have MIR emission similar to Seyfert galaxies. Normal AGN optical/UV continua are needed for Seyferts to produce their MIR luminosity, thus ruling out lacking an optical/UV continuum as the reason for their optical dullness.

We use the luminosity at 6 μm to investigate the MIR regime of the spectrum. This should also help separate the effects of dust from host galaxy and torus components, as MIR emission from AGN is produced by torus dust being heated by UV photons.

We investigate the scaling between MIR luminosity at 6 μm and obscuration-corrected X-ray luminosity, as discussed in Chen et al. (2017). This relation is constructed from a Levenberg–Marquardt minimized χ^2 fitting to AGN populations from the Boötes, XMM-COSMOS, XRT-SDSS, and XXL-N samples assuming a bilinear, broken power-law fit. We note that the "breaking luminosity" of this relation is at $L_{\mu m} = 44.79$ erg s^{-1}, which is brighter than our most luminous object at 6 μm.

Additionally, Fiore et al. (2009) and Gandhi et al. (2009) established an intrinsic MIR–to–X-ray relationship. Gandhi et al. (2009) used high-resolution photometry of local Seyfert galaxies to find that they follow the same correlation of Compton-thick AGN. The work of Fiore et al. (2009) searched for highly obscured, Compton-thick AGN to estimate the missing fraction of AGN that should be observed in these systems. In doing so, they estimated unobscured X-ray luminosities for sources that they originally detected in the MIR.

We plot this relation against our variable X-ray AGN candidates in Figure 9. The luminosity at 6 μm is estimated from our SED models. We find some of the BPT AGN and absorption line–dominated systems to be generally consistent with the X-ray–to–MIR relation. This suggests that at least some of the optically dull AGN in our sample have typical AGN optical/UV continuum and torus dust emission.

On the other hand, some of the objects in our sample do have excess MIR emission compared to their X-ray luminosity. These include four spectroscopic AGN, two of the absorption line systems, composite objects, and some objects without optical spectroscopy. These objects could have excess dust near the nucleus, potentially explaining the optical dullness in some cases. As MIR emission can be an indirect tracer of AGN power (Lansbury et al. 2015), this can point to the effect of obscuration within these systems. The X-ray absorption causes

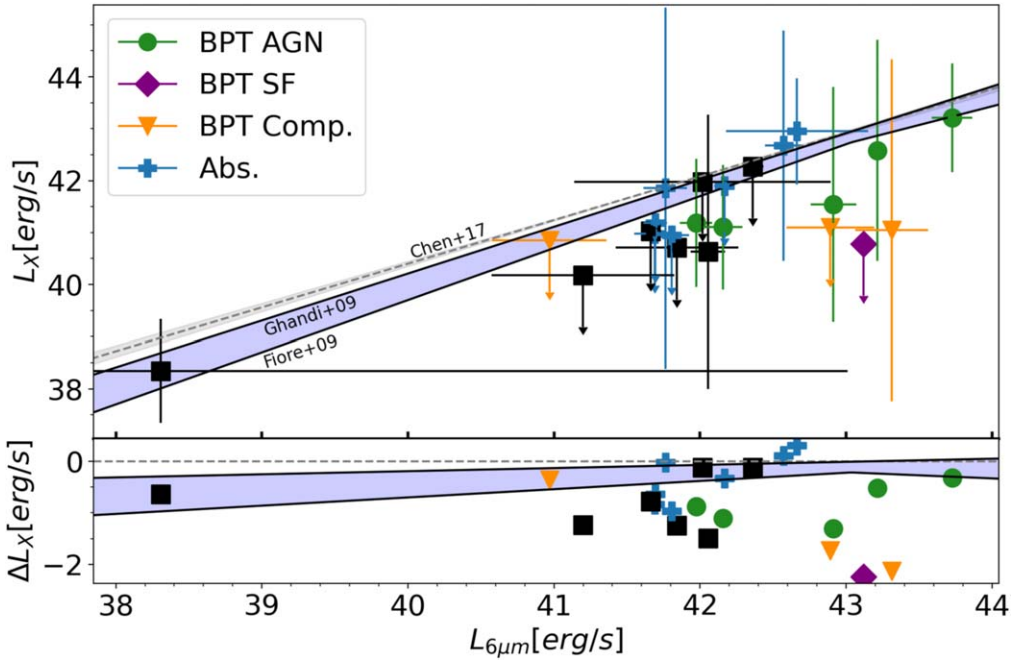

Figure 9. Plot of 2–10 keV luminosity vs. luminosity at 6 μm. The gray line and shaded region show the empirical relation and its uncertainty from Chen et al. (2017). The intrinsic relationships of Fiore et al. (2009) and Gandhi et al. (2009) are given as solid black lines, with the blue shaded area representing a range of possible intrinsic and unabsorbed X-ray luminosities for the given MIR power. Residuals relative to the Chen et al. (2017) relation are again given in the bottom panel. Marker shapes and colors are the same as in Figure 5.

a steeper slope in the fitting, thus causing some of our spectroscopic AGN to fall below these literary relations.

6. Conclusions

In this work, we measured X-ray emission for 23 UV variability–selected AGN candidates from Wasleske et al. (2022) using archival CXO and XMM observations. We detected X-ray emission from 11 of these objects. Then, we constructed SED models using `X-CIGALE` (Yang et al. 2020) to measure contributions from dust, stars, and gas across the electromagnetic spectrum. We then explored the reasons why this sample displays a diversity of optical spectroscopic signatures. We summarize our main findings as follows.

1. We measure X-ray emission for 23 sources originally selected as AGN candidates from their UV variability (Wasleske et al. 2022). Eleven of the 23 are detected.
2. We compare our observed X-ray luminosities to those expected due to star formation. We find that 10/11 detected galaxies have X-ray luminosities of more than 0.6 dex above the Ranalli et al. (2003) $L_{\text{X-ray}}$–SFR relation (this is the criterion used for AGN selection in Agostino et al. 2023). This suggests that these systems are bona fide AGN. The upper limits for the remaining objects are not constraining enough to rule out the presence of AGN.
3. Three sources, NSA 64146, 64272, and 64286, have detections in both CXO and XMM observations. We argue that the consistency of the X-ray emission over years-long timescales is more consistent with an AGN than a TDE as the possible cause of the X-ray emission and the significant UV variability.
4. One source, NSA 208625, has bright X-ray emission in CXO observations taken in 2005 and a nondetection in XMM observations taken in 2015. The source faded by at least an order of magnitude over the decade. This could suggest a changing-state AGN or a TDE in this galaxy.
5. Our confirmed AGN show a diversity of optical spectroscopic properties. We use results from SED modeling to study whether stellar or dust emission could impact the optical spectroscopic properties. We find the following.
   (a) The absorption line–dominated systems generally have a higher ratio of stellar-to-AGN luminosities. This is consistent with a scenario where host galaxy light dominates the optical spectrum.
   (b) The BPT AGN are in generally good agreement with the relationship of α_{OX} to luminosity at 2500 Å from Just et al. (2007). Other objects show large deviations from this relationship, suggesting possible physical differences from luminous quasars. Obscuring material blocking X-ray emission from the innermost part of the AGN's accretion disk could be responsible for the nonspectroscopic AGN deviating from the relation.
   (c) We find excess dust luminosity in those objects in our sample lacking optical spectroscopic signatures.
   (d) We also find excess MIR emission for some objects in our sample, possibly from the heating of dust or host galaxy contamination.

Ultimately, there is no one clear scenario that explains the diversity of optical spectroscopic properties in this sample. Dilution of AGN signatures by star formation, galaxy-wide dust extinction, and nuclear dust extinction are likely all at play to different degrees in different galaxies. Spatially resolved spectroscopy and more detailed spectral fitting would help to

further understand the diversity of properties in this interesting sample.

The variability selection of candidates done in Wasleske et al. (2022) was complemented by spectroscopic analysis, IR AGN selection, and low-resolution SED modeling without X-ray values. This work has expanded on that analysis by including X-ray information and more detailed SED modeling. The results here clearly demonstrate that variability is a robust AGN selection technique, identifying objects that would not have been selected based on their optical spectroscopic properties.

Acknowledgments

We thank Erin Kimbro for helpful comments.

This research has made use of data obtained from the 4XMM XMM-Newton Serendipitous Source Catalog compiled by the 10 institutes of the XMM-Newton Survey Science Centre selected by ESA.

This research has made use of data obtained from the Chandra Data Archive and the Chandra Source Catalog, and software provided by the Chandra X-ray Center (CXC) in the application packages CIAO and Sherpa.

Funding for the SDSS and SDSS-II has been provided by the Alfred P. Sloan Foundation, the Participating Institutions, the National Science Foundation, the U.S. Department of Energy, the National Aeronautics and Space Administration, the Japanese Monbukagakusho, the Max Planck Society, and the Higher Education Funding Council for England. The SDSS Web Site is http://www.sdss.org/. The SDSS is managed by the Astrophysical Research Consortium for the Participating Institutions. The Participating Institutions are the American Museum of Natural History, Astrophysical Institute Potsdam, University of Basel, University of Cambridge, Case Western Reserve University, University of Chicago, Drexel University, Fermilab, the Institute for Advanced Study, the Japan Participation Group, Johns Hopkins University, the Joint Institute for Nuclear Astrophysics, the Kavli Institute for Particle Astrophysics and Cosmology, the Korean Scientist Group, the Chinese Academy of Sciences (LAMOST), Los Alamos National Laboratory, the Max Planck Institute for Astronomy (MPIA), the Max Planck Institute for Astrophysics (MPA), New Mexico State University, Ohio State University, University of Pittsburgh, University of Portsmouth, Princeton University, the United States Naval Observatory, and the University of Washington.

Facilities: GALEX, SDSS, UKIRT, WISE, FLWO:2MASS.

Software: Astropy (The Astropy Collaboration 2018).

Appendix
Example SED Models

In Figure 10 below, we give examples of SED modeling of X-CIGALE for NSA 28616 and NSA 64129. Models for stellar attenuated, stellar unattenuated, nebular, dust, and AGN emission are given in yellow, blue, green, red, and orange, respectively. The total model is shown in black with model fluxes as red dots and observed fluxes as purple circles.

Both objects' SED modeling has significant AGN contributions in the IR. The model for NSA 28616 shows extinction of the AGN emission at higher energies. In the X-ray portion of this SED, the total model line, given in black, is completely equivalent to the AGN emission model line. The model for NSA 64129 shows heavy extinction in the ultraviolet.

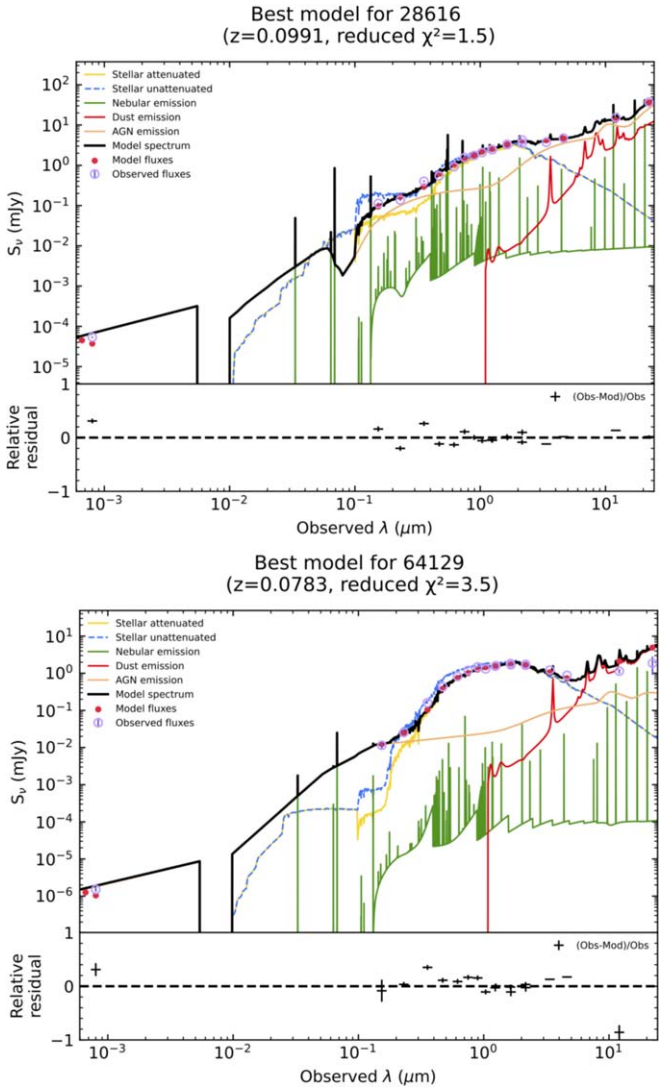

Figure 10. SED models of NSA 28616 (top) and NSA 64129 (bottom).

ORCID iDs

Erik J. Wasleske https://orcid.org/0000-0003-3986-9427
Vivienne F. Baldassare https://orcid.org/0000-0003-4703-7276

References

Agostino, C. J., & Salim, S. 2019, ApJ, 876, 12
Agostino, C. J., Salim, S., Ellison, S. L., Bickley, R. W., & Faber, S. M. 2023, ApJ, 943, 174
Agostino, C. J., Salim, S., Faber, S. M., et al. 2021, ApJ, 922, 156
Ahumada, R., Prieto, C. A., Almeida, A., et al. 2020, ApJS, 249, 3
Asmus, D., Gandhi, P., Hönig, S. F., Smette, A., & Duschl, W. J. 2015, MNRAS, 454, 766
Astropy Collaboration, Price-Whelan, A. M., Sipőcz, B. M., et al. 2018, AJ, 156, 123
Baldassare, V. F., Geha, M., & Greene, J. 2018, ApJ, 868, 152
Baldassare, V. F., Geha, M., & Greene, J. 2020, ApJ, 896, 10
Baldassare, V. F., Reines, A. E., Gallo, E., et al. 2016, ApJ, 829, 57
Baldassare, V. F., Reines, A. E., Gallo, E., & Greene, J. E. 2017, ApJ, 836, 20
Baldwin, J. A., Phillips, M. M., & Terlevich, R. 1981, PASP, 93, 5
Birchall, K. L., Watson, M. G., & Aird, J. 2020, MNRAS, 492, 2268
Blanton, M. R., & Moustakas, J. 2009, ARA&A, 47, 159
Brandt, W., & Hasinger, G. 2005, ARA&A, 43, 827
Bruzual, G., & Charlot, S. 2003, MNRAS, 344, 1000

Burke, C. J., Liu, X., Chen, Y.-C., Shen, Y., & Guo, H. 2021, MNRAS, 504, 543
Calzetti, D., Armus, L., Bohlin, R. C., et al. 2000, ApJ, 533, 682
Cao, R., Liu, F. K., Zhou, Z. Q., Komossa, S., & Ho, L. C. 2018, MNRAS, 480, 2929
Carroll, C. M., Hickox, R. C., Masini, A., et al. 2021, ApJ, 908, 185
Chabrier, G. 2003, PASP, 115, 763
Charalampopoulos, P., Pursiainen, M., Leloudas, G., et al. 2023, A&A, 673, A95
Chen, C.-T. J., Hickox, R. C., Goulding, A. D., et al. 2017, ApJ, 847, 145
Desroches, L.-B., Greene, J. E., & Ho, L. C. 2009, ApJ, 698, 1515
Dong, X.-B., Ho, L. C., Yuan, W., et al. 2012, ApJ, 755, 167
Donley, J. L., Koekemoer, A. M., Brusa, M., et al. 2012, ApJ, 748, 142
Draine, B. T., Aniano, G., Krause, O., et al. 2013, ApJ, 780, 172
Evans, I. N., Primini, F. A., Miller, J. B., et al. 2020, AAS Meeting Abstracts, 235, 154
Filippenko, A. V. 1997, ARA&A, 35, 309
Fiore, F., Puccetti, S., Brusa, M., et al. 2009, ApJ, 693, 447
Gandhi, P., Horst, H., Smette, A., et al. 2009, A&A, 502, 457
Gezari, S. 2021, ARA&A, 59, 21
Gezari, S., Martin, D. C., Forster, K., et al. 2013, ApJ, 766, 60
Greene, J. E., & Ho, L. C. 2004, ApJ, 610, 722
Greene, J. E., & Ho, L. C. 2007, ApJ, 656, 84
Hainline, K. N., Reines, A. E., Greene, J. E., & Stern, D. 2016, ApJ, 832, 119
Hickox, R. C., & Alexander, D. M. 2018, ARA&A, 56, 625
Ho, L. C., Filippenko, A. V., & Sargent, W. L. W. 1997, ApJS, 112, 315
Inoue, A. K. 2011, MNRAS, 415, 2920
Just, D. W., Brandt, W. N., Shemmer, O., et al. 2007, ApJ, 665, 1004
Kirkpatrick, A., Pope, A., Sajina, A., et al. 2015, ApJ, 814, 9
Komossa, S., Zhou, H., Wang, T., et al. 2008, ApJL, 678, L13
Lambrides, E. L., Chiaberge, M., Heckman, T., et al. 2020, ApJ, 897, 160
Landt, H., Bentz, M. C., Ward, M. J., et al. 2008, ApJS, 174, 282
Lang, D. 2014, AJ, 147, 108
Lansbury, G. B., Gandhi, P., Alexander, D. M., et al. 2015, ApJ, 809, 115
Lawrence, A., Warren, S. J., Almaini, O., et al. 2007, MNRAS, 379, 1599
Lemons, S. M., Reines, A. E., Plotkin, R. M., Gallo, E., & Greene, J. E. 2015, ApJ, 805, 12
Lutz, D., Maiolino, R., Spoon, H. W. W., & Moorwood, A. F. M. 2004, A&A, 418, 465
Magorrian, J., Tremaine, S., Richstone, D., et al. 1998, AJ, 115, 2285
Maller, A. H., Berlind, A. A., Blanton, M. R., & Hogg, D. W. 2009, ApJ, 691, 394
Messick, A., Baldassare, V. F., Geha, M., & Greene, J. E. 2023, arXiv:2306.15775
Molina, M., Reines, A. E., Latimer, C. J., Baldassare, V., & Salehirad, S. 2021, ApJ, 922, 155
Moran, E. C., Shahinyan, K., Sugarman, H. R., Vélez, D. O., & Eracleous, M. 2014, AJ, 148, 136
Natarajan, P. 2014, GReGr, 46, 1702
Pfeifle, R. W., Ricci, C., Boorman, P. G., et al. 2022, ApJS, 261, 3
Plotkin, R. M., Gallo, E., Haardt, F., et al. 2016, ApJ, 825, 139
Pritchard, T. A., Roming, P. W. A., Brown, P. J., et al. 2012, ApJ, 750, 128
Ranalli, P., Comastri, A., & Setti, G. 2003, A&A, 399, 39
Rees, M. J. 1988, Natur, 333, 523
Reines, A. E., Condon, J. J., Darling, J., & Greene, J. E. 2020, ApJ, 888, 36
Reines, A. E., Greene, J. E., & Geha, M. 2013, ApJ, 775, 116
Rigby, J. R., Rieke, G. H., Donley, J. L., Alonso-Herrero, A., & Pérez-González, P. G. 2006, ApJ, 645, 115
Rosen, S. R., Webb, N. A., Watson, M. G., et al. 2016, A&A, 590, A1
Skrutskie, M. F., Cutri, R. M., Stiening, R., et al. 2006, AJ, 131, 1163
Stalevski, M., Fritz, J., Baes, M., Nakos, T., & Popović, L. 2012, MNRAS, 420, 2756
Stalevski, M., Ricci, C., Ueda, Y., et al. 2016, MNRAS, 458, 2288
Stern, D. 2015, ApJ, 807, 129
Strubbe, L. E., & Quataert, E. 2009, MNRAS, 400, 2070
Villarroel, B., & Korn, A. J. 2014, NatPh, 10, 417
Volonteri, M. 2010, A&ARv, 18, 279
Volonteri, M., Lodato, G., & Natarajan, P. 2008, MNRAS, 383, 1079
Wang, T.-G., Zhou, H.-Y., Komossa, S., et al. 2012, ApJ, 749, 115
Wasleske, E. J., Baldassare, V. F., & Carroll, C. M. 2022, ApJ, 933, 37
Watson, M. G., Schröder, A. C., Fyfe, D., et al. 2009, A&A, 493, 339
Webb, N. A., Coriat, M., Traulsen, I., et al. 2020, A&A, 641, A136
Wright, E. L., Eisenhardt, P. R. M., Mainzer, A. K., et al. 2010, AJ, 140, 1868
Yan, R., Ho, L. C., Newman, J. A., et al. 2011, ApJ, 728, 38
Yang, G., Boquien, M., Brandt, W. N., et al. 2022, ApJ, 927, 192
Yang, G., Boquien, M., Buat, V., et al. 2020, MNRAS, 491, 740
Zhu, G., Blanton, M. R., & Moustakas, J. 2010, ApJ, 722, 491